

EFFICIENT PROTON TRANSPORT MODELLING FOR PROTON BEAM THERAPY AND BIOLOGICAL QUANTIFICATION

BEN S. ASHBY¹, VERONIKA CHRONHOLM², DANIEL K. HAJNAL², ALEX LUKYANOV³,
KATHERINE MACKENZIE¹, AARON PIM², AND TRISTAN PRYER^{1,2}

ABSTRACT. In this work, we present a fundamental mathematical model for proton transport, tailored to capture the key physical processes underpinning Proton Beam Therapy (PBT). The model provides a robust and computationally efficient framework for exploring various aspects of PBT, including dose delivery, linear energy transfer, treatment planning and the evaluation of relative biological effectiveness. Our findings highlight the potential of this model as a complementary tool to more complex and computationally intensive simulation techniques currently used in clinical practice.

1. INTRODUCTION

Proton Beam Therapy (PBT) has emerged as an important modality in the treatment of specific challenging cancers, particularly where conventional photon-based radiotherapy struggles to minimise irradiation to surrounding critical tissues. Pediatric cancers, skull base tumours, and complex head and neck malignancies are example cases where PBT offers a distinct advantage due to its ability to deposit energy with precision, peaking at the Bragg peak, see Figure 1.

The Bragg peak enables precise targeting of tumours while sparing adjacent healthy tissue, making PBT an attractive option for complex clinical scenarios. However, despite its potential for superior dose profiles, there are fundamental challenges in treatment planning, verification, and uncertainty quantification. A key issue is the variability in patient anatomy during the treatment course, such as changes in water retention or tumour motion, which can lead to suboptimal tumour coverage or increased irradiation of healthy tissues. These challenges limit the potential of PBT to achieve superior therapeutic outcomes consistently.

Moreover, the intricacies of Relative Biological Effectiveness (RBE), which varies with proton energy and penetration depth, add a layer of complexity to treatment optimisation. The RBE, a measure of the relative damage caused by protons compared to photons, depends heavily on Linear Energy Transfer (LET), the rate at which energy is deposited along the proton track. Regions with higher LET are known to cause more complex and clustered DNA damage, which is harder for cells to repair, leading to increased biological effectiveness. This correlation makes LET a key metric for linking physical dose distributions to biological outcomes. As highlighted by Nystrom et al. [1]:

“We believe that the endless discussions of which is the most appropriate RBE-model and the exact values of the RBE for different tissue and in different parts of the dose distribution should be put on hold. Rather, efforts should be put in the development of clinically useful tools to visualise LET distributions and the possibility to include LET in the optimisation of proton treatment plans.”

This sentiment underscores the urgent need for practical, clinically-relevant methodologies to optimise PBT treatment plans while navigating biological complexities. In this work, we adopt

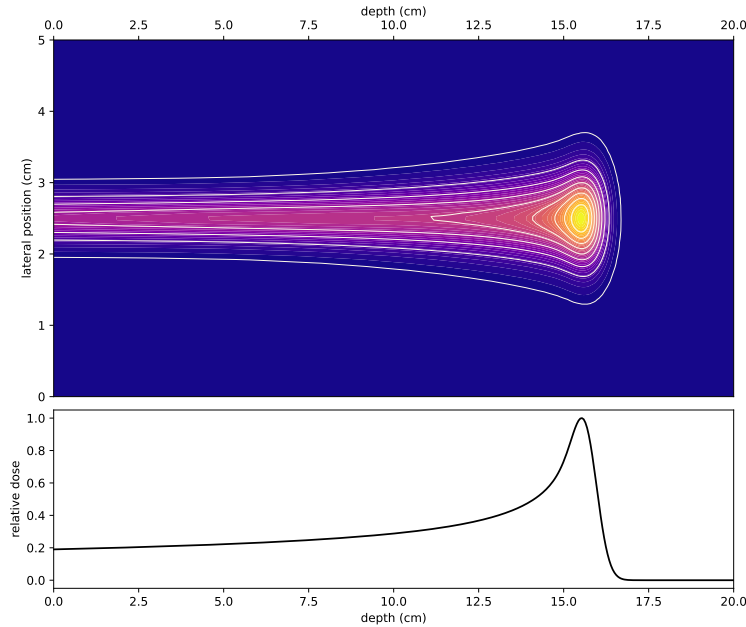


FIGURE 1. Simulated dose profile of a proton beam illustrating the Bragg peak. The simulation was performed using MCsquare with $1.21 \cdot 10^7$ particles, a beam width of 2 mm, without nuclear interactions. The initial proton energy is 150 MeV with a 1% energy spread, and the dose is integrated along the plane orthogonal to the beam axis.

a fundamental mathematical perspective to address some of these challenges in PBT treatment planning. Specifically, we focus on developing a robust and accessible framework for optimising dose distribution, incorporating considerations of RBE and its impact on tumour cell survival. A particular emphasis is placed on LET, enabling the integration of biological metrics into the optimisation process.

Our approach introduces:

- A simplified, yet precise, model that facilitates rapid exploration of treatment plan precision and its implications for therapeutic outcomes.
- A rigorous, accessible, mathematical formulation for optimising the biological effective dose, explicitly accounting for LET distributions and RBE variability.
- A biologically informed framework for interpreting treatment plans, incorporating cell survival fraction and RBE as key metrics.
- A detailed sensitivity analysis of the proposed framework, identifying the main parameters that influence treatment outcomes.

The goal is to provide tools that are not only theoretically sound but also practical for clinical implementation, bridging the gap between mathematical modelling and real-world PBT optimisation. This framework supports investigations towards personalised and adaptive therapy strategies, with

the end goal of enhancing precision in challenging clinical scenarios by enabling the integration of spatially resolved biological metrics, such as LET, into treatment planning.

Modelling proton transport and dose distribution in PBT has traditionally relied on Monte Carlo simulations [2, 3], which provide detailed physical insights but come with significant computational costs [4]. These methods remain the gold standard for accuracy but are impractical for real-time treatment planning. Recent advancements in neural network-based methodologies show promise for accelerating dose prediction by leveraging large datasets [5, 6]. However, these approaches are still nascent in clinical contexts and require extensive validation.

From a biological perspective, the role of RBE in treatment optimisation has been an important point of research. Unlike photon radiotherapy, where energy independence simplifies the calculation of biologically effective dose (BED) [7], proton radiotherapy demands careful calibration to account for RBE variability with depth and energy [8]. While multiple RBE models exist, the lack of consensus on their clinical applicability continues to pose challenges, and in practice virtually all treatment centres use a constant RBE of 1.1 [9, 10, 11, 12], despite the fact that there is broad consensus that RBE varies along the particle track, increasing near the Bragg peak [13] to values significantly larger than 1.1. Indeed, RBE typically reaches values of approximately 1.6 in the falloff region of the Bragg peak [14].

Finally, efforts to incorporate LET distributions into treatment planning are gaining traction (see [4] for an example). These efforts align with the broader push toward integrating data-driven methodologies, such as neural networks, which have shown promise in accelerating dose prediction and enhancing planning workflows. Our framework complements such approaches by offering a rigorous and interpretable model for evaluating and validating biologically informed treatment plans, as well as providing tools to visualise the effect that varying optimisation routines to include additional quantities such as LET has upon the final plan.

It is worth noting that treatment planning is only one aspect of the broader radiotherapy workflow, which encompasses tumour growth modelling, temporal variations and interactions with other treatment modalities such as chemotherapy. While these dynamic aspects can be addressed using optimal control formulations [15], this work focuses on stationary problems, providing a foundational framework that enables the capture of key physical and biological processes. In clinical practice, temporal changes such as tumour shrinkage or movement are addressed through adaptive radiotherapy, which relies on re-imaging, re-planning, or pre-optimised scenarios to ensure treatment quality across long, fractionated courses of therapy [16].

In this context, the computational efficiency of our framework offers a significant advantage, particularly in adaptive workflows where rapid dose calculations and fast treatment plan optimisations are important. In this work we aim to bridge the gap between theoretical modelling and clinical applicability, laying the groundwork for examining biological metrics in current planning workflows.

The rest of this paper is structured as follows: in §2, we introduce the fundamental mathematical model, describing the principles of charged particle transport, stopping power, and LET and validate the model against existing Monte Carlo codes. In §3, we shift focus to biological metrics, exploring how the model can incorporate key measures such as the cell survival fraction and RBE to evaluate the biological effectiveness of proton beams. §4 addresses model uncertainties, providing a sensitivity analysis to quantify how variations in key parameters affect dose and LET predictions. Finally, §5 explores applications to treatment planning, demonstrating how the framework can optimise dose delivery and integrate biological metrics to enhance therapeutic outcomes.

2. MODELLING OF CHARGED PARTICLE TRANSPORT

In this section we introduce fundamental modelling concepts in proton transport and discuss a fundamental model to aid in the exploration of the ideas discussed here.

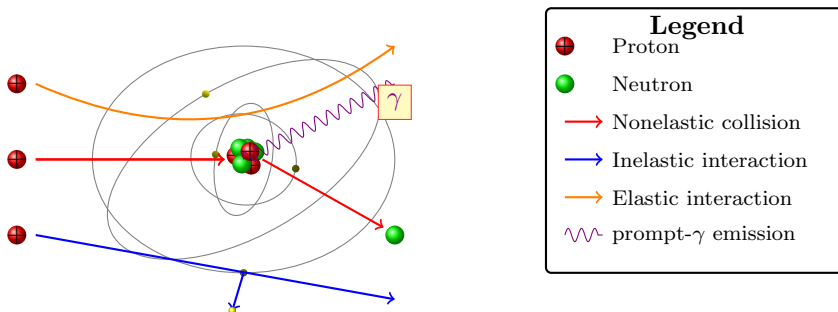


FIGURE 2. *The three main interactions of a proton with matter. A **nonelastic** proton-nucleus collision, an **inelastic** Coulomb interaction with atomic electrons and **elastic** Coulomb scattering with the nucleus.*

2.1. A model for proton transport. In this section, we introduce a simplified model for proton transport that builds upon the fundamental principles shown in Figure 2. To that end, consider a bounded domain $X \subset \mathbb{R}^3$. For $0 < E_{\min} < E_{\max}$, we define the interval $I = [E_{\min}, E_{\max}]$ as the set of admissible particle energies and let \mathbb{S}^2 represent the unit sphere, which describes possible particle trajectories.

At any given position $\mathbf{x} \in X$, with energy $E \in I$ and a trajectory direction $\boldsymbol{\omega} \in \mathbb{S}^2$, we are interested in modelling the particle fluence. The fluence, denoted $\psi(\mathbf{x}, E, \boldsymbol{\omega})$, describes the differential number of particles passing through a small surface area within an infinitesimal energy range. We let \mathcal{S} denote the *stopping power*, formally defined in §2.3, as a function of the particle energy in a homogeneous domain. To simplify the analysis, we assume that angular scattering of the particles is minimal, that nonelastic collisions are rare. Based on these assumptions, we arrive at a transport model where the fluence satisfies

$$(1) \quad \boldsymbol{\omega} \cdot \nabla_{\mathbf{x}} \psi(\mathbf{x}, E, \boldsymbol{\omega}) + \frac{\partial}{\partial E} (\mathcal{S}(\mathbf{x}, E) \psi(\mathbf{x}, E, \boldsymbol{\omega})) = 0.$$

This equation captures the balance between the particle's motion through the medium and the energy loss through ionisation described by the stopping power.

Boundary conditions are required to close the model. The inflow condition specifies the fluence at the boundary of the domain

$$(2) \quad \partial X_- := \{\mathbf{x} \in \partial X : \mathbf{n}(\mathbf{x}) \cdot \boldsymbol{\omega} < 0\}$$

where particles enter, while the energy cutoff condition ensures that no particles exist above the maximum energy, these read

$$(3) \quad \begin{aligned} \psi(\mathbf{x}, E, \boldsymbol{\omega}) &= \mathcal{G}(\mathbf{x}, E, \boldsymbol{\omega}) \quad \forall \mathbf{x} \in \partial X_-, E \in I \\ \psi(\mathbf{x}, E_{\max}, \boldsymbol{\omega}) &= 0 \quad \forall \mathbf{x} \in X, \boldsymbol{\omega} \in \mathbb{S}^2. \end{aligned}$$

This formulation provides the foundation we use to explore proton transport.

2.2. **Model simplification.** Given the assumptions made, it is useful to consider the variable

$$(4) \quad z := (\mathbf{x} - \mathbf{x}_0) \cdot \boldsymbol{\omega},$$

where $\mathbf{x}_0 \in \partial X_-$ is a given entrance point and $\boldsymbol{\omega} \in \mathbb{S}^2$ is a given trajectory. We define

$$(5) \quad z_{\max} := \inf \{s > 0 : \mathbf{x}_0 + s\boldsymbol{\omega} \in \partial X, \mathbf{n}(\mathbf{x}_0 + s\boldsymbol{\omega}) \cdot \boldsymbol{\omega} > 0\},$$

which, for a given entrance point, represents the minimal path length to an outflow boundary. Then, for fixed \mathbf{x}_0 and $\boldsymbol{\omega}$, we define the one-dimensional stopping power and fluence in terms of the energy E and the one-dimensional track length z by the following change of variables,

$$(6) \quad \begin{aligned} S(z, E) &:= \mathcal{S}(\mathbf{x}_0 + z\boldsymbol{\omega}, E) \\ u(z, E) &:= \psi(\mathbf{x}_0 + z\boldsymbol{\omega}, E, \boldsymbol{\omega}) \\ g(E) &:= \mathcal{G}(\mathbf{x}_0, E, \boldsymbol{\omega}). \end{aligned}$$

We obtain the following problem for u :

$$(7) \quad \frac{\partial}{\partial z} u(z, E) + \frac{\partial}{\partial E} (S(z, E)u(z, E)) = 0, \quad \forall z, E \in (0, z_{\max}) \times I,$$

subject to the boundary conditions

$$(8) \quad \begin{aligned} u(0, E) &= g(E), \quad \forall E \in I, \\ u(z, E_{\max}) &= 0, \quad \forall z \in (0, z_{\max}). \end{aligned}$$

Figure 3 gives a visualisation of the domain and inflow boundaries.

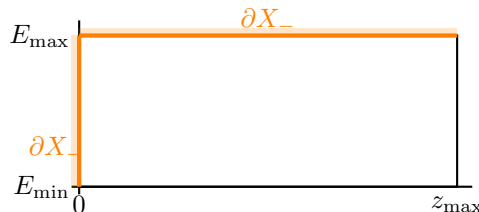


FIGURE 3. An illustration of the domain and the relevant inflow boundary.

2.3. **Energy, range & stopping power.** Suppose that a proton beam consisting of particles of a single energy E_0 enter a medium. There is a fundamental relationship between E_0 (in MeV) and the range R_0 the protons penetrate into the medium. This relationship is often modelled as a power law

$$(9) \quad R_0 = \alpha E_0^p,$$

where $p \in [1, 2]$ and $\alpha > 0$ is related to the mass density of the medium. Some indicative empirical values are given in Table 1.

From this relationship, one can derive a formula for the remaining energy $E(z)$ at a given depth, $z \geq 0$ by observing that at depth z , the range of the beam is $R_0 - z$. Applying the range-energy relationship (9) at this depth yields

$$(10) \quad R_0 - z = \alpha E(z)^p,$$

Medium	p	α
Water	1.75 ± 0.02	0.00246 ± 0.00025
Muscle	1.75	0.0021
Bone	1.77	0.0011
Lung	1.74	0.0033

TABLE 1. Range-Energy relationship parameters for different media. Notice the parameter p remains relatively constant across different biological media. In contrast, the parameter α varies more significantly, as it is strongly dependent on the density and composition of each medium. The uncertainty in the water phantom is based on comparing three parameterisations of the Bragg Kleeman rule from [17, 18, 19].

Solving for E we see

$$(11) \quad E(z) = \alpha^{-\frac{1}{p}} (R_0 - z)^{\frac{1}{p}}.$$

This expression describes the energy of the proton beam as a function of depth. The linear stopping power, defined as the energy loss per unit distance travelled, can then be computed by

$$(12) \quad S(z) := -\frac{dE(z)}{dx} = \frac{\alpha^{-\frac{1}{p}}}{p} (R_0 - z)^{\frac{1}{p}-1}.$$

Finally, since the relationship (11) is invertible for $0 \leq z \leq R_0$, the stopping power can be expressed in terms of energy:

$$(13) \quad S(E) = \frac{1}{\alpha p} E^{1-p}.$$

This representation, called the Bragg-Kleeman rule, illustrates how the stopping power decreases as a function of energy which is the property that yields the forward facing peaked nature of the Bragg peak.

2.4. Remark (Relativistic effects). *Proton therapy typically uses proton energies in the range of 50 to 250 MeV. While these energies are high enough to require accurate modeling of stopping power, they are not so high that relativistic effects dominate. In this intermediate energy range, the Bragg-Kleeman model provides a sufficiently accurate approximation of stopping power while maintaining simplicity and computational efficiency [20].*

The Bethe-Bloch formula, illustrated in Figure 4, is more precise at relativistic speeds as it incorporates corrections and additional parameters necessary at very high energies [21]. However, it also introduces complexity to calculations and exhibits unphysical behaviour at low energy levels, making it less suitable for the energy ranges used in proton therapy.

2.5. Closed form solution. Due to the form of the stopping power, the equation is hyperbolic in nature, we can therefore use the method of characteristics to construct a closed form solution. To that end, the characteristic curves satisfy

$$(14) \quad E^p = E_{\max}^p - \frac{z}{\alpha}.$$

This curve represents the energy trajectory of a monoenergetic proton beam with initial energy E_{\max} in the (z, E) -plane. Integrating (7) along these characteristic curves, the solution for fluence

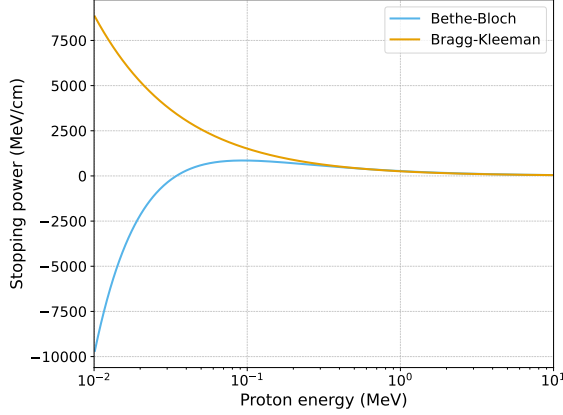


FIGURE 4. Stopping power as a function of energy for the Bragg-Kleeman and Bethe-Bloch models. The two models show good agreement in the intermediate energy range relevant to proton therapy however differ dramatically in the low energy range.

$u(z, E)$ is

$$(15) \quad u(z, E) = \left(E^p + \frac{z}{\alpha}\right)^{\frac{1-p}{p}} g\left(\left(E^p + \frac{z}{\alpha}\right)^{\frac{1}{p}}\right) E^{p-1}.$$

2.6. Computation of Absorbed Dose. The absorbed dose, $D(z)$, represents the energy deposited per unit mass at a given depth and can be calculated by integrating the stopping power weighted by the particle fluence over the energy range

$$(16) \quad \begin{aligned} D(z) &= \int_{E_{\min}}^{E_{\max}} \frac{S(E)}{\rho(x)} u(z, E) dE \\ &= \frac{1}{\alpha p} \frac{1}{\rho(z)} \int_{E_{\min}}^{E_{\max}} \left(E^p + \frac{z}{\alpha}\right)^{\frac{1-p}{p}} g\left(\left(E^p + \frac{z}{\alpha}\right)^{\frac{1}{p}}\right) dE. \end{aligned}$$

This formulation captures the full spectrum of proton energies within I , accounting for their interactions with the medium and the resulting energy deposition.

To provide an intuitive understanding of this setup, Figure 5 presents a visualisation of the fluence and resulting dose for a 62 MeV proton beam with a 1% energy spread. The figure consists of a grid of panels illustrating three components:

- The initial energy distribution $g(E)$ of the proton beam is shown on the left, highlighting the Gaussian profile centred at 62 MeV.
- The middle panel depicts the fluence in depth-energy space, demonstrating how the protons' energy evolves along their trajectories as they penetrate the medium.
- The bottom panel shows the resulting dose $D(z)$, plotted as a function of depth, capturing the energy deposited within the target region.

This visualisation effectively connects the initial beam properties to the resulting dose distribution within the context of (16).

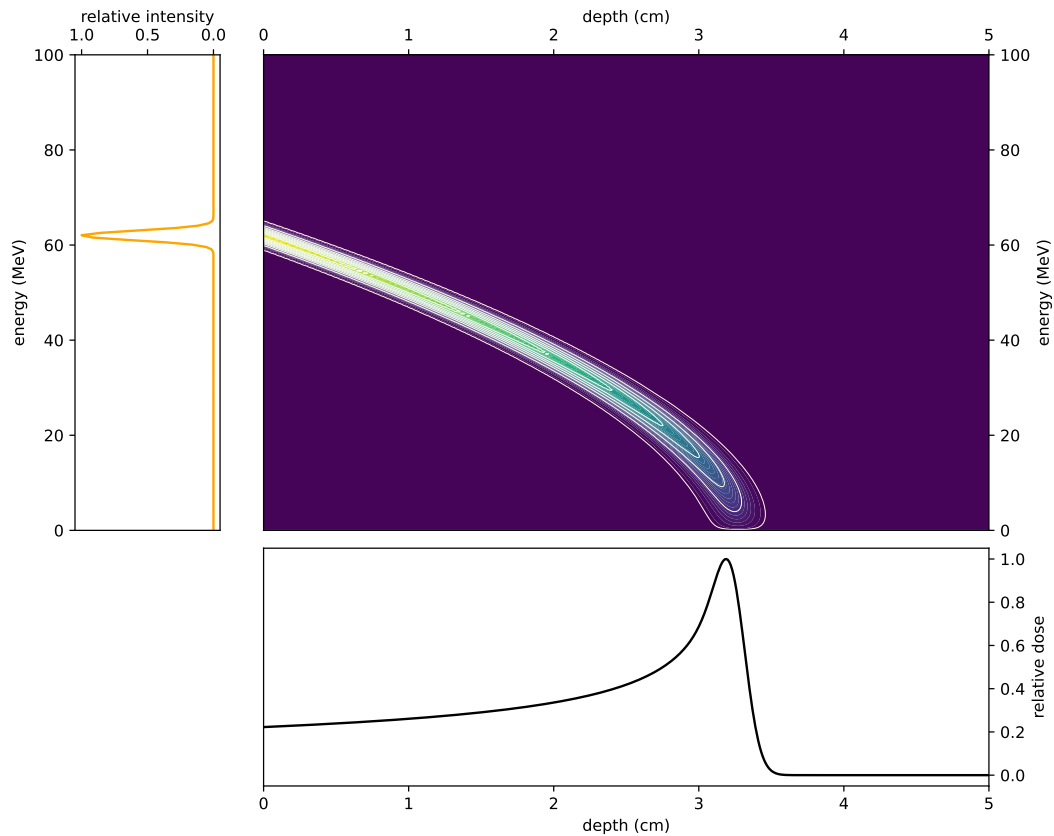


FIGURE 5. A visualisation of dose calculation. Left: the initial Gaussian energy profile of a 62 MeV proton beam with a 1% energy spread. Middle: the fluence in depth-energy space, illustrating how the beam evolves as it travels through the medium. Bottom: the resultant dose as a function of depth.

2.7. Linear Energy Transfer. A related concept to stopping power is the Linear Energy Transfer (LET), which describes the energy locally absorbed by the medium per unit distance. The physical definition from the ICRU [22] defines LET, or the restricted linear electronic stopping power as

$$(17) \quad L_{\Delta} = \frac{dE_{\Delta}}{dz},$$

which represents the energy lost dE_{Δ} by the primary charged particle in interactions with electrons, along a distance dz minus energy carried away by energetic secondary electrons having initial kinetic energies greater than Δ . In the limit $\Delta \rightarrow \infty$, LET is equivalent to the stopping power, this is referred to as the unrestricted LET. Essentially, stopping power accounts for the total energy loss, while LET focuses on the energy absorbed locally in the medium, which will be important in understanding the biological impact of radiation later in this work.

If we assume that all of the energy lost is absorbed locally by the material, then we have two notions of calculating the average LET from the particle fluence: track-averaged and dose-averaged [23].

Track-averaged LET.

$$(18) \quad L_T(z) = \frac{\int_E u(z, E) S(E) dE}{\int_E u(z, E) dE}.$$

Dose-averaged LET.

$$(19) \quad L_D(z) = \frac{\int_E u(z, E) S^2(E) dE}{\int_E u(z, E) S(E) dE}.$$

2.8. Remark (Monoenergetic simplification). *The track-averaged LET is sometimes referred to as fluence-averaged or particle-averaged LET. Track- and dose-averaged LET are defined for a polyenergetic beam, where $g(E)$ is an arbitrary distribution of energies. However, in the case of a truly monoenergetic beam, where*

$$(20) \quad g(E) = c\delta(E - E_0)$$

for some constant c and initial energy $E_0 \in \mathbb{R}$, the expressions for track-averaged and dose-averaged LET simplify to

$$(21) \quad L_T(z) = L_D(z) = S\left(\left(E_0^p - \frac{z}{\alpha}\right)^{\frac{1}{p}}\right).$$

2.9. Comparison with Monte Carlo Codes. This section compares the analytical model described above with established simulation tools to validate its performance against key benchmarks. Specifically, we evaluate whether the simplified model, given by Equation 7, can accurately reproduce both qualitatively correct and quantitatively reasonable behaviour. The comparison is conducted against the Monte Carlo simulation tool MCsquare [24] and the Geant4-based TOPAS framework [25].

To assess the accuracy of the one-dimensional analytical model, we consider a pristine Bragg peak simulation as a computational benchmark. A mono-energetic proton beam with an initial energy of $E_0 = 62$ MeV and a fluence of 1.21 gigaprotons/cm² is used as the input beam. The analytical model employs standard Bragg-Kleeman parameter values for water ($\alpha = 2.2 \times 10^{-3}$, $p = 1.77$) as reported in [19], while the Monte Carlo codes use their respective default material parameters for water. To account for the energy spread in the Monte Carlo simulations, the standard deviation of the proton energy spectrum is set to ϵE_0 , with $\epsilon = 0.01$.

The boundary condition for the analytical model is defined as:

$$(22) \quad u(0, E) = 1.21 \times 10^9 \times C \exp\left(-\frac{(E - E_0)^2}{2\epsilon^2 E_0^2}\right),$$

where C is a normalisation constant ensuring that the integral of the spectrum matches the total fluence of 1.21 gigaprotons/cm².

For the Monte Carlo codes, a three-dimensional water phantom is simulated and the depth-dose curve is obtained by integrating the dose over the plane perpendicular to the beam axis. Depth-dose curves for the analytical model are computed using Equation 16.

The comparison results are shown in Figure 6, where close agreement between the models can be observed. The left panel shows results excluding nuclear interactions in the Monte Carlo simulations, while the right panel includes these effects. Both cases demonstrate that the analytical

model captures the depth-dose behaviour with high fidelity, providing a computationally efficient alternative to Monte Carlo simulations.

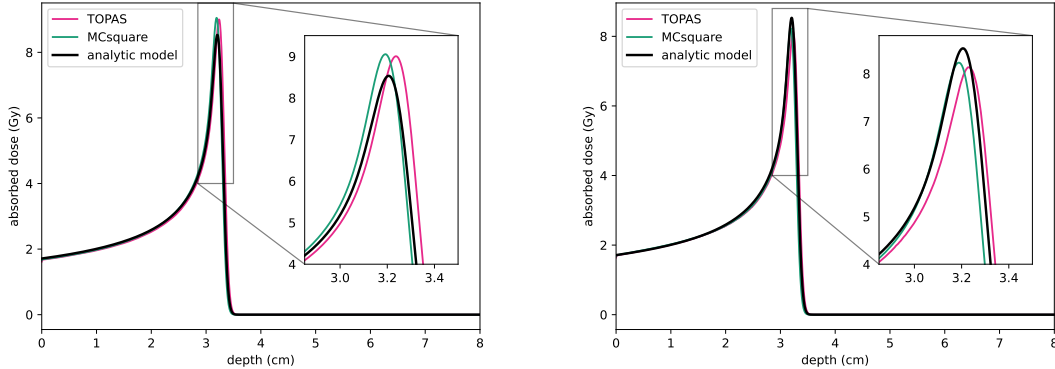


FIGURE 6. Comparison of depth-dose curves for a 62 MeV mono-energetic proton beam in water obtained from the one-dimensional analytical model (black), MCsquare (green) and TOPAS (pink). Left: nuclear interactions are excluded in the Monte Carlo simulations. Right: nuclear interactions are included. All simulations are scaled such that the total number of incoming protons is 1.21 gigaprotons, ensuring a consistent comparison of absorbed dose.

3. BIOLOGICAL METRICS

Treatment planning can be thought of as translating a physician’s prescription into a set of parameters that define the radiotherapy delivered to a patient [26]. The treatment plan should be ‘optimal’ in some sense, as defined in Section 5. Typically, the goal is to deliver a dose that closely matches a prescribed target dose profile using a suitable metric. Absorbed dose is widely used for this purpose because it is measurable and can be computed accurately in numerical simulations. In addition, prescriptions from clinicians are given as a dose due to the long history of use and gathered expertise in photon based radiotherapy. However, dose is only a proxy for biological effect and there is no simple one-to-one relationship between absorbed dose and biological outcomes [1]. For example, LET and cell type must also be considered, and for this reason, metrics beyond dose have been incorporated into carbon ion beam treatment planning (where LET plays a larger role than for protons) for over two decades [27, 28, 29]. In this section, we focus on cell survival rates as a biological metric to assess treatment plan quality and introduce the concept of the relative biological effectiveness (RBE) for proton beams, as well as the biological dose (BD).

To formalise these ideas, specific examples of biological effect must be considered. The choice of metric should align with the desired clinical endpoints and be measurable or detectable [29]. Examples of such endpoints include tumour control probability (TCP) and normal tissue complication probability (NTCP), which are often estimated from *in vivo* experiments. For simplicity, we focus on the cell survival fraction, a quantity measurable *in vitro* via clonogenic assay [30]. A cell is considered ‘killed’ or inactive if it is unable to proliferate. This metric provides an objective measure of treatment efficacy while avoiding the complexities of more comprehensive metrics like TCP.

However, while the survival fraction is relevant for tumour control, it may not be an ideal measure for toxicity in healthy tissues [1], which is an important consideration in treatment planning.

For X-rays, the survival fraction $\mathcal{SF}_{\text{X-ray}}$ is accurately modelled in vitro as a function of absorbed dose $D_{\text{X-ray}}(x)$ using the *linear-quadratic model* [31]:

$$(23) \quad \mathcal{SF}_{\text{X-ray}}(z; D_{\text{X-ray}}) = \exp(-c_{\text{X-ray}}(z)D_{\text{X-ray}}(z) - \beta_{\text{X-ray}}(z)D_{\text{X-ray}}(z)^2),$$

where $c_{\text{X-ray}}(z)$ ¹ and $\beta_{\text{X-ray}}(z)$ are model parameters typically estimated through regression, with their dependence on cell species captured via their spatial variation. We note that the linear quadratic model becomes less accurate in some regimes [32], but is effective in many practical dose ranges.

3.1. Remark (Interpretation of the parameters in the linear-quadratic model). *As described in [33], the parameters in the linear-quadratic model have physical interpretations. Cell death following irradiation is primarily caused by DNA double-strand breaks, either from a single particle interaction or from two single-strand breaks created by separate interactions. The parameters $c_{\text{X-ray}}(z)$ and $\beta_{\text{X-ray}}(z)$ correspond to the expected number of single and double-strand breaks per unit dose, respectively. While a general derivation of the model is given in [31], the parameters are often determined empirically by fitting the model to experimental data.*

3.2. Linear-Quadratic Model for Protons. Equation (23) implies a one-to-one relationship between absorbed dose and cell killing. Predicting cell survival following irradiation with proton beams is more complex than for X-rays due to the additional dependence on LET. This dependence can be incorporated into the linear-quadratic (LQ) framework and many studies have investigated how LET affects the parameters of the LQ model [34, 35, 36]. LET-dependent models remain widely used and well-studied [37, 8].

Experimental evidence suggests that, within clinically relevant LET ranges, the coefficient c depends approximately linearly on LET:

$$(24) \quad c(z; L_D) = c_0(z) + \lambda(z)L_D(z),$$

where $c_0(z)$ corresponds to the value of c for X-rays and $\lambda(z)$ represents the tissue-dependent LET sensitivity. A more detailed model in [38] (see also [39]) proposes modifying this dependence based on the ratio of $c_{\text{X-ray}}$ to $\beta_{\text{X-ray}}$, introducing exponential dependence when this ratio is large. However, for simplicity, we assume $\lambda(z)$ is constant for a given tissue type.

The relationship between β and LET is less clear and constant β is commonly assumed [8]. This assumption aligns with the theory of dual radiation action. Nevertheless, some studies, such as [40], have examined potential LET-dependent variations in β .

Following Chaudhary et al. [8], we set $c_0 = c_{\text{X-ray}}$ in Equation 24. The spatial variation of $c_{\text{X-ray}}$, β and λ reflects tissue-specific responses to radiation. Table 2 summarises these parameters for two cell types: AG01522 (skin cells) and U87 (malignant brain tumour cells) [8].

The survival fraction of cells irradiated by a proton dose D and LET L_D is then given by:

$$(25) \quad \mathcal{SF}(z; D, L_D) = \exp(-c(z; L_D) \cdot D(z) - \beta(z)D(z)^2).$$

For a given dose profile, $D(z)$, the surviving fraction of cells at each depth z may be predicted by the model (25). An example for a Bragg peak is shown in Figure 7. It is worth noting that this model may require further modification for heavier charged particles such as carbon ions [37].

¹Often denoted as α in the literature, but here denoted c to avoid confusion with parameters in the Bragg-Kleeman model.

Cell Type	$c_{X\text{-ray}}$ [Gy^{-1}]	λ [$\mu\text{m keV}^{-1} \text{Gy}^{-1}$]	β [Gy^{-2}]
AG01522 (skin)	0.54 ± 0.06	0.0451	0.051 ± 0.038
U87 (brain tumour)	0.11 ± 0.028	0.0127	0.059 ± 0.024

TABLE 2. Parameters for the LET-dependent LQ model (25), measured for two cell types [8].

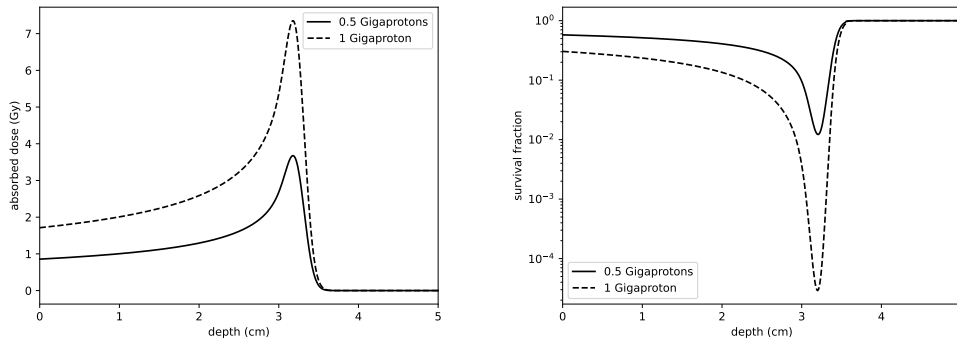


FIGURE 7. Left: depth-dose profiles for 62 MeV proton beams of two different intensities, Right: corresponding survival fractions of cells against depth assuming a homogeneous medium of cells, computed using the model (25).

3.3. Relative Biological Effectiveness. Relative Biological Effectiveness (RBE) is an important metric in radiobiology, defined as the ratio of doses required from two radiation sources to achieve the same biological effect. It captures differences in energy deposition and clinical outcomes between radiation modalities [12]. Here, we consider RBE in terms of cell survival fraction.

Proton beams differ from X-rays in their energy deposition characteristics. In particular, low-energy protons near the distal end of their range inflict greater biological damage on tissue. In [13], an increase in molecular markers of double-strand DNA breaks (γH2AX foci) is observed at the distal end of the Bragg peak, consistent with Remark 3.1. It is well known that the RBE of protons exceeds 1.0 and a constant value of 1.1 has been widely adopted in clinical practice [9, 10, 11, 12]. While some studies support this approximation, others suggest it is insufficient [38].

Quantifying RBE is important to fully exploit the advantages of proton therapy. However, this task is challenging due to complex dependencies on biological factors, including cell type, cell cycle phase [10] and clinical endpoint [12], as well as limited data for many tissues [41]. Results from in vitro experiments on specific cell lines often do not generalise to others due to significant biological variation. Additionally, RBE depends on dose and radiation quality, typically characterised by LET [37].

In this work, we consider a spatially variable notion of relative biological effectiveness as follows. Given a depth dose curve $D(z)$ and LET profile $L_D(z)$, at each point z a surviving fraction of cells may be computed as described above. The equivalent photon dose, i.e. the dose that yields the same cell survival fraction, is found by inverting the functional relationship given in Equation (23).

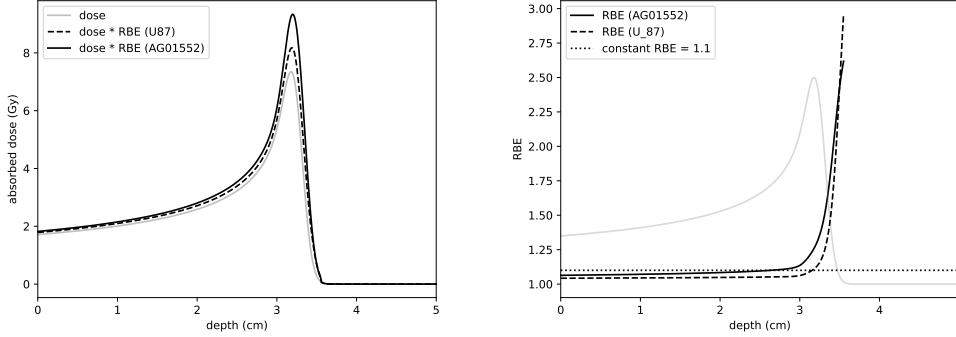


FIGURE 8. Left: RBE-weighted dose curves for a 62 MeV mono-energetic proton beam in water phantom, calculated using the TDRA model for cell survival and parameters from [8] for AG01522 and U87 cell lines. Right: Corresponding RBE. Dose curve illustrates RBE behaviour along the Bragg peak and is not to scale.

Specifically, given D , we seek $D_{X\text{-ray}}$ such that:

$$(26) \quad \mathcal{SF}(z; D(z), L_D(z)) = \mathcal{SF}_{X\text{-ray}}(z; D_{X\text{-ray}}(z))$$

for all z . We may then define a spatially variable relative biological effectiveness as

$$(27) \quad RBE(z, D, L_D) := \frac{D_{X\text{-ray}}(z)}{D(z)}.$$

The RBE-weighted dose is then defined to be the product of dose and RBE, i.e. precisely the equivalent X-ray dose $D_{X\text{-ray}}$. This quantity can be used to compare the biological effect with photon dose curves. RBE and RBE-weighted dose curves are shown in Figure 8 for two different cell types studied in [8]. We observe that the RBE is in line with the clinical value of 1.1 up until the Bragg peak, but becomes significantly larger in the distal falloff region.

3.4. Biological Dose (BD). Unfortunately, optimising for dose delivery that results in a given survival fraction is problematic for a number of reasons. Discussion of these issues is postponed until §5. In this section an alternative is presented which is more amenable to optimisation.

A natural alternative is to consider the logarithm of the survival fraction, as is common in log-likelihood maximisation. This idea appears in [4, 42], where the LET-weighted dose, often referred to as the biological dose (BD), is used as an optimisation metric. In [4, Appendix A], a discussion of a simpler linear exponential model for the survival fraction is used is given. It can be viewed as a simplification of the linear quadratic model for which fractionation effects are neglected. The model is given by:

$$(28) \quad \mathcal{SF}_{\text{lin}}(z; D(z), L_D(z)) := \exp(-c(z; L_D)D(z)).$$

The biological dose is then defined as

$$(29) \quad BD(z) := -\log(\mathcal{SF}_{\text{lin}}(z; D(z), L_D(z))) / c_{X\text{-ray}} = D(z) \left(1 + \frac{\lambda}{c_{X\text{-ray}}} L_D(z) \right),$$

where $D(z)$ is the absorbed dose, $L_D(z)$ is the dose-averaged LET, and $\lambda/c_{X\text{-ray}}$ quantifies the contribution of LET to the biological effect (cf. Equations (24) & (25)). This formulation balances

physical dose delivery with biological considerations, making it a promising metric for treatment planning.

4. MODEL UNCERTAINTIES AND SENSITIVITY

This section aims to quantify the uncertainty in the magnitude and position of $D(z)$ (16) when the stopping power parameters α and p from the Bragg-Kleeman rule in Equation 13 are uncertain. Specifically, we consider the dose as parameterised by α and p , such that $D(z) = D(z; \alpha, p)$. Two methods, an active subspace approach and a Monte Carlo simulation, are implemented to analyse the impact of uncertainty in the model.

4.1. Active Subspace Method. We apply an active subspace method to evaluate the relative importance of the parameters α and p over specified ranges. This approach involves examining the dose across the phase space of α and p at a fixed point in the domain. The direction perpendicular to the contour lines in this space indicates the path along which the greatest change in dose occurs, providing insight into the relative sensitivities of $D(z; \alpha, p)$ to α and p . Furthermore, the orientation of these contour lines is orthogonal to the eigenvectors of the covariance matrix at that point (see [43, §10.5] for further details).

The parameters α and p are modelled as independent normally distributed random variables, with means (μ_α, μ_p) and variances $(\sigma_\alpha, \sigma_p)$:

$$(30) \quad \begin{aligned} \alpha &\sim \mathcal{N}(\mu_\alpha, \sigma_\alpha) \\ p &\sim \mathcal{N}(\mu_p, \sigma_p). \end{aligned}$$

For all simulations, we take $\mu_\alpha = 0.00246$ and $\mu_p = 1.75$, as shown in Table 1.

We consider three cases for the standard deviations σ_α and σ_p : absolute values, relative values, and empirical estimates based on data. For the absolute case, we set $\sigma_\alpha = \sigma_p = 0.0001$. For the relative case, σ_α and σ_p are taken to be 1% of their respective mean values. For the empirical case, we use the data from Table 1, assuming the 95% confidence intervals represent twice the standard deviation. Thus, σ_α and σ_p are scaled by $1/1.96$ to align the normal distribution with these intervals. Table 3 summarises these choices.

Case	σ_α	σ_p
Absolute	0.0001	0.0001
Relative	0.0000246	0.0175
Empirical	0.000128	0.0102

TABLE 3. Standard deviations σ_α and σ_p for the three case studies.

A sensitivity analysis is conducted at three points in the domain, labelled A , B , and C , as shown in Figure 9. Point A lies midway between the start of the beam and the Bragg peak, point B is at the Bragg peak, and point C is at the location of the steepest gradient.

Contour plots illustrating the sensitivities at points A , B , and C are shown in Figures 10, 11, and 12, respectively. The x - and y -axes of these figures represent the ranges $(\mu_\alpha - 2\sigma_\alpha, \mu_\alpha + 2\sigma_\alpha)$ and $(\mu_p - 2\sigma_p, \mu_p + 2\sigma_p)$, ensuring that α and p span their 95% confidence intervals.

Figure 10 illustrates that, when absolute uncertainties are considered, the contour lines are nearly vertical, indicating that $D(x; \alpha, p)$ is significantly more sensitive to changes in α than to equivalent changes in p . In contrast, Figure 11 shows that when relative uncertainties are used, a 1% change

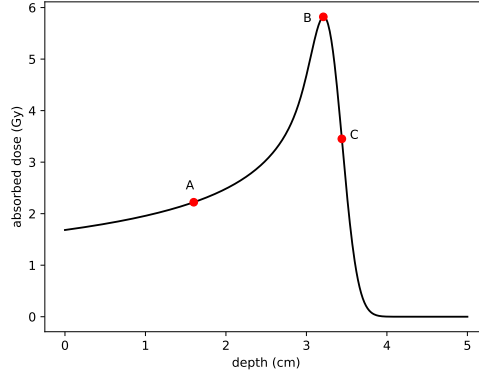


FIGURE 9. Positions for the active subspace analysis. Point A is halfway between the start and the Bragg peak, point B is at the peak, and point C is at the position with the steepest gradient. The initial beam has an energy of 62MeV, with a spread of 5%.

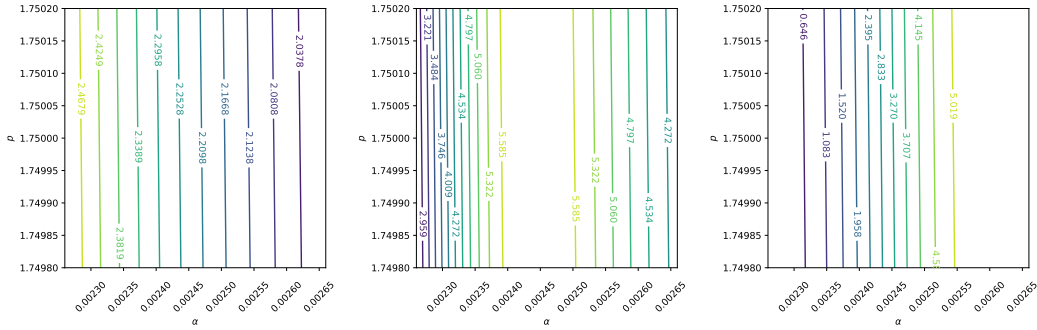


FIGURE 10. Contour plot of dose at points A , B , and C when α and p are assumed to follow normal distributions with absolute standard deviations $\sigma_\alpha = \sigma_p = 0.0001$.

in p has a greater impact on $D(x; \alpha, p)$ than a 1% change in α . Finally, Figure 12, which uses empirical standard deviations based on Table 1, demonstrates that $D(x; \alpha, p)$ is equally sensitive to both parameters over the examined phase plane.

It is important to note that while Figure 10 highlights α 's greater influence under absolute uncertainties and Figure 11 shows p 's dominance under relative uncertainties, Figure 12 reflects a balance in sensitivity when using empirically motivated standard deviations. This motivates the inclusion of uncertainty in both α and p in the subsequent Monte Carlo analysis.

4.2. Monte Carlo Simulation. In this section, we investigate how uncertainty in the stopping power parameters α and p affects the shape and position of the dose curve $D(z; \alpha, p)$. Using Monte Carlo simulations, we quantify the overall uncertainty in $D(z; \alpha, p)$ as well as the uncertainty in the depth of the Bragg peak. As in subsection 4.1, we model α and p as independent, normally

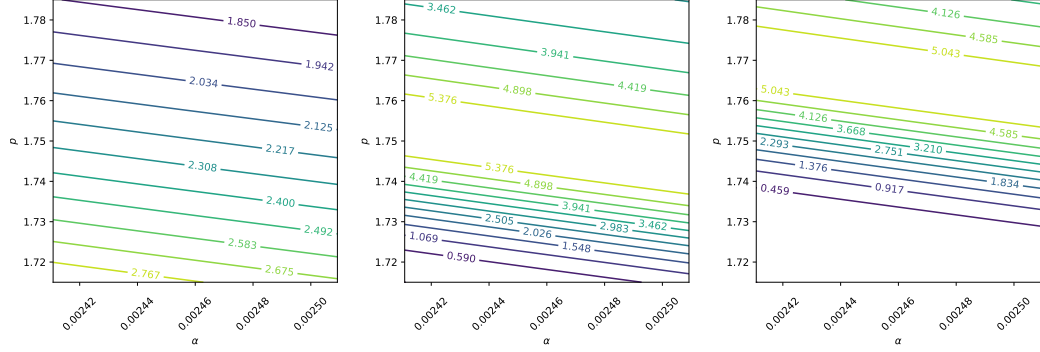


FIGURE 11. Contour plot of dose at points A, B, and C when α and p are assumed to follow normal distributions with relative standard deviations $\sigma_\alpha = 0.01\mu_\alpha = 0.0175$ and $\sigma_p = 0.01\mu_p = 0.0000246$.

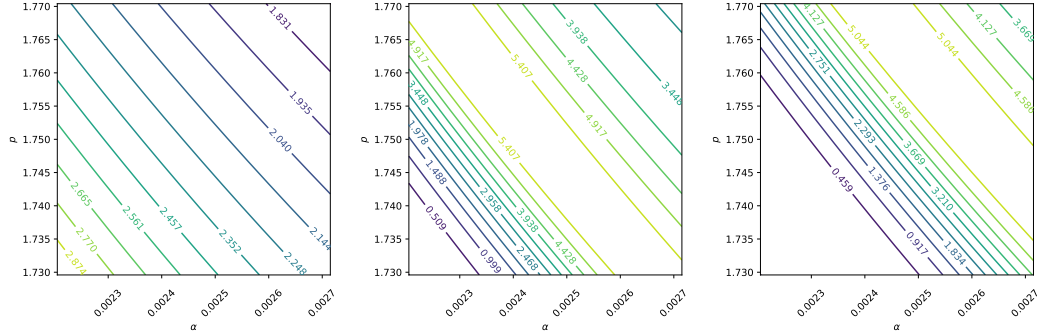


FIGURE 12. Contour plot of dose at points A, B, and C when α and p are assumed to follow normal distributions with empirical standard deviations $\sigma_\alpha = 0.000128$ and $\sigma_p = 0.0102$.

distributed random variables with means (μ_α, μ_p) and standard deviations $(\sigma_\alpha, \sigma_p)$. Specifically, we take $\mu_\alpha = 0.00246$ and $\mu_p = 1.75$, and use empirical standard deviations $\sigma_\alpha = 0.000128$ and $\sigma_p = 0.0102$, corresponding to 95% confidence intervals.

The nominal dose curve, computed with $\alpha = \mu_\alpha$ and $p = \mu_p$, is denoted as $D^*(z; \mu_\alpha, \mu_p)$ and serves as the “true” reference dose curve. This curve corresponds to the assumed parameter values $\mu_\alpha = 0.00246$ and $\mu_p = 1.75$, as presented in Table 1. In the figures that follow, $D^*(z; \mu_\alpha, \mu_p)$ is included to illustrate how uncertainties in α and p influence the dose curve.

It is important to note that the nominal dose curve $D^*(z; \mu_\alpha, \mu_p)$ is not equivalent to the mean dose curve, as $D^*(z; \mathbb{E}[\alpha], \mathbb{E}[p]) \neq \mathbb{E}[D(z, \alpha, p)]$. As a result, the nominal dose curve does not necessarily lie within the calculated confidence intervals, which reflect the distribution of $D(z; \alpha, p)$. This underscores the impact of parameter uncertainty on the dose curve and highlights the importance of considering the full range of variability in α and p .

In Figure 13, we show how the dose curve changes when α and p deviate by one or two standard deviations in either the positive or negative direction. The results indicate that deviations in either

α or p alone induce moderate changes in $D(z; \alpha, p)$. However, simultaneous deviations in both parameters cause larger changes in both the magnitude and the location of the Bragg peak.

Notably, the probability of both α and p being off by 2σ simultaneously is significantly lower than the probability of a single parameter deviating by 2σ , assuming independence. For instance, under the normal distribution assumption, the probability of α being off by $2\sigma_\alpha$ is 5%, while the probability of simultaneous 2σ deviations for both parameters is 0.25%.

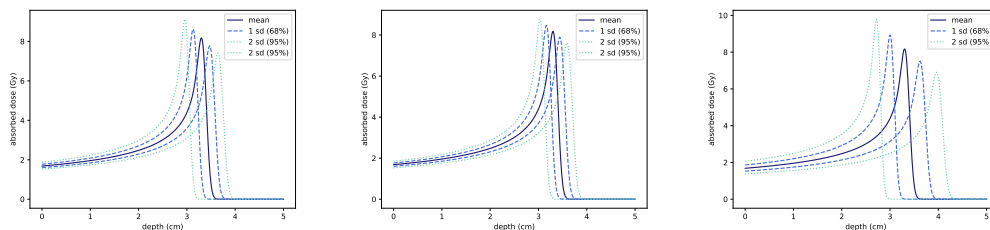


FIGURE 13. Sensitivity of $D(z; \alpha, p)$ to under- and overestimation of α and p by one or two standard deviations. The nominal dose curve $D^*(z; \mu_\alpha, \mu_p)$ is shown for reference. On the left, only α has been under- or overestimated; in the centre only p ; and on the right both α and p .

Figure 14 presents the estimated 68% and 95% confidence intervals for the dose curve $D(z; \alpha, p)$. These intervals are derived using a Monte Carlo approach, with 25,000 independent random samples of α and p . Empirical quantiles are computed at each depth z to generate the ensemble of dose curves.

The results show that introducing uncertainty in either α or p individually leads to similar confidence intervals. However, when uncertainty is included for both parameters simultaneously, the confidence intervals for the dose curve become significantly larger. This demonstrates that the combined uncertainties in α and p amplify the overall uncertainty in dose deposition, emphasising the importance of accurately characterising both parameters.

In Figure 15, we show the estimated 68% and 95% confidence intervals for the peak position z_{peak} of the dose curve. These intervals are also derived using a Monte Carlo approach with 25,000 independent random samples of α and p .

The results indicate that the confidence intervals for z_{peak} are comparable in magnitude when uncertainty is included for either α or p alone. However, when both parameters are simultaneously uncertain, the confidence intervals for z_{peak} are considerably larger, consistent with the shifts in z_{peak} observed in Figure 13. Even relatively small uncertainties in α and p result in a 95% confidence interval for z_{peak} of approximately ± 1 cm, a level of uncertainty significant for treatment planning. This highlights the need for precise parameter estimation to ensure accurate dose delivery.

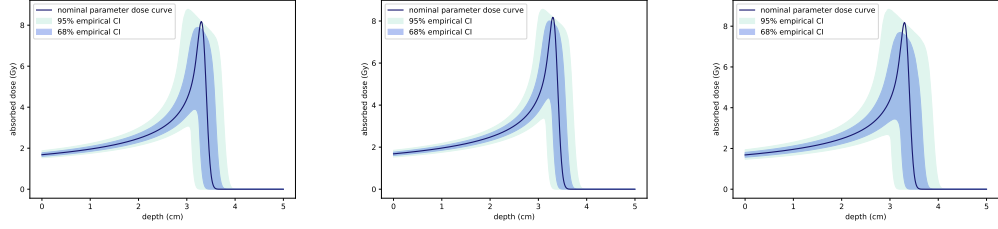


FIGURE 14. Confidence intervals for the variation in dose $D(z; \alpha, p)$ when α and p are normally distributed with means $\mu_\alpha = 0.00246, \mu_p = 1.75$ and standard deviations $\sigma_\alpha = 0.000128, \sigma_p = 0.0102$. The nominal dose curve $D(z; \mu_\alpha, \mu_p)$, resulting from the assumed parameter values μ_α and μ_p , is plotted in dark blue. The 68% and 95% confidence intervals are shown as shaded regions, estimated using 25,000 independent random samples of α and p . On the left, only uncertainty in α has been included; in the centre only uncertainty in p , and on the right uncertainty in both α and p .

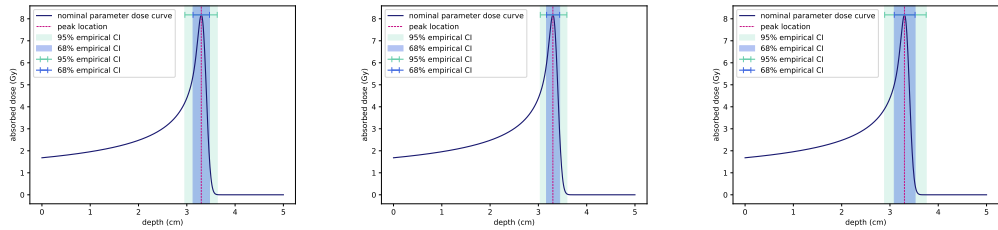


FIGURE 15. Confidence intervals for the variation in peak depth z_{peak} when α and p are normally distributed with means $\mu_\alpha = 0.00246, \mu_p = 1.75$ and standard deviations $\sigma_\alpha = 0.000128, \sigma_p = 0.0102$. The nominal dose curve $D(z; \mu_\alpha, \mu_p)$, resulting from the assumed parameter values μ_α and μ_p , is plotted in dark blue. The corresponding nominal peak depth of the curve $D(z; \mu_\alpha, \mu_p)$ is plotted as a dashed red line. The 68% and 95% confidence intervals for z_{peak} are shown as shaded regions, estimated using 25,000 independent random samples of α and p . On the left, only uncertainty in α has been included; in the centre only uncertainty in p , and on the right uncertainty in both α and p .

5. TREATMENT PLANNING

To complete our study, we now examine how the model developed can be applied to treatment planning in proton therapy.

The goal of treatment planning is to determine the optimal initial beam angles, intensities, and energies such that the dose delivered to a cancerous region is maximised while minimising the biological damage to surrounding healthy tissues. This objective can be framed as a control problem.

Efficient optimisation methods are crucial in Intensity-Modulated Proton Therapy (IMPT), where practitioners often generate multiple treatment plans along an approximate Pareto surface to balance competing objectives and select the most suitable plan for the patient. Furthermore, the optimisation of proton therapy treatment plans involves a significantly larger number of decision parameters compared to Intensity-Modulated Radiation Therapy (IMRT) [44].

5.1. Dose Optimisation as a Constrained Least Squares Problem. We consider the spatial domain divided into disjoint regions of healthy and tumourous tissues, denoted Ω_H and Ω_T , respectively. For simplicity, we assume $\Omega_T = [z_{\text{prox}}, z_{\text{dist}}]$. Given a target dose profile $T(x)$, the objective is to construct an input beam $g : [E_{\text{min}}, E_{\text{max}}] \rightarrow \mathbb{R}$ such that the resulting dose $D(z)$ closely approximates $T(z)$.

To approach this problem, we require:

- A discrete representation of the input beam g ;
- A forward model $g \rightarrow D$ to predict the dose profile;
- A metric to quantify the difference between $D(z)$ and $T(z)$.

To represent the input beam, we assume it is a superposition of a finite set of Gaussian-shaped basis beams, φ_i , $i = 1, \dots, N_y$, each centred at a principal energy E_i with variance σ_i^2 . This formulation reduces the space of possible input functions g to a finite-dimensional vector space spanned by the basis beams:

$$(31) \quad g(\mathbf{y}, E) = \sum_{i=1}^{N_y} y_i \varphi_i(E),$$

where $\mathbf{y} = (y_1, \dots, y_{N_y})$ represents the weights or intensities of each constituent beam. Each φ_i approximates a mono-energetic beam, and the choice of Gaussian-shaped beams ensures practical feasibility given equipment constraints, as discussed in [45]. Alternative representations, such as piecewise constant or linear approximations, may lead to input beams that are difficult to realise in practice.

The forward model is provided by the one-dimensional analytical model from §2, which is linear with respect to the initial beam energy g . This allows the total dose profile to be expressed as a linear combination of precomputed dose profiles $D_i(z)$ corresponding to unit-intensity beams:

$$(32) \quad D(\mathbf{y}, z) = \sum_{i=1}^{N_y} y_i D_i(z).$$

By precomputing the dose profiles $D_i(z)$ for each basis beam φ_i , the optimisation problem is reduced to finding the optimal coefficients \mathbf{y} , which is computationally efficient.

To measure how well $D(\mathbf{y}, z)$ approximates $T(z)$, we define a cost function that penalises deviations between the dose and the target. Let $w(z)$ be a non-negative weighting function, then the cost functional is

$$(33) \quad l(\mathbf{y}) := \int_X w(z) (D(\mathbf{y}, z) - T(z))^2 dx.$$

For practical implementation, we evaluate the dose at a finite set of points z_0, \dots, z_{N_x} and approximate the integral using the composite trapezoidal rule. This leads to the discrete cost functional

$$(34) \quad L(\mathbf{y}) := \sum_{j=1}^{N_x} \frac{1}{2} w(z_j) (D(\mathbf{y}, z_j) - T(z_j))^2 (z_j - z_{j-1}).$$

5.2. Definition (Treatment planning optimisation problem). Given beams $\varphi_1, \dots, \varphi_{N_y}$, target and weighting functions T, w , and an admissible set Y , find $\mathbf{y} \in Y$ such that:

$$(35) \quad L(\mathbf{y}) \leq L(\mathbf{y}') \quad \forall \mathbf{y}' \in Y.$$

5.3. Remark (Weighting function w). The weighting function w provides flexibility in defining the cost function, allowing different priorities in the treatment plan. We illustrate this with the following examples:

- (1) In the simplest case, where the goal is to deliver a specified dose to a target region Ω_T with no restrictions elsewhere, w can be set as the indicator function of Ω_T :

$$(36) \quad w = \mathbb{1}_{\Omega_T}.$$

- (2) When additional considerations, such as sparing an organ at risk (OAR) within $\Omega_O \subseteq \Omega_H$, are required, the weighting function can assign different priorities to regions. For example:

$$(37) \quad w(z) = \begin{cases} w_T & \text{for } z \in \Omega_T, \\ w_O & \text{for } z \in \Omega_O, \\ w_H & \text{otherwise.} \end{cases}$$

Here, setting $w_O \gg w_T$ reflects a higher priority for sparing the OAR over achieving the target dose in the tumour.

5.4. Remark (Admissible set Y). The admissible set Y allows the inclusion of practical constraints on beam intensities. For instance, beams must have non-negative intensity, so Y must satisfy:

$$(38) \quad Y \subseteq \{\mathbf{y} \in \mathbb{R}^{N_y} : y_i \geq 0 \quad \forall i\}.$$

Additionally, upper bounds on intensity may be enforced due to equipment limitations or safety constraints.

Selection of the Inflow Energy Profiles. The success of the optimisation problem in 5.2 depends on appropriate choices for the beam profiles φ_i and the admissible set Y . Physically, it is desirable for the spread-out Bragg peak (SOBP) to cover the tumour region Ω_T . This requires the ranges of the constituent beams φ_i to lie within Ω_T .

The range of a proton beam, determined by the Bragg-Kleeman rule (see Equation (9)), can be inverted to compute the energy E of protons with a given range R :

$$(39) \quad E = \left(\frac{R}{\alpha}\right)^{1/p}.$$

This relationship allows the selection of principal energies (the centres of the Gaussian profiles for each beam) such that the ranges satisfy:

$$(40) \quad z_{\text{prox}} \leq \alpha E_i^p \leq z_{\text{dist}}.$$

The choice of beam principal energies and widths significantly affects the appearance of the resulting SOBP. As illustrated in Figure 17, restricting all beam ranges to lie strictly within the tumour region can lead to oscillations at the distal end of the SOBP. These oscillations persist even when the boundary condition is resolved with a greater number of beams. Allowing some beams with energies E_i such that $R(E_i) > z_{\text{dist}}$ reduces these oscillations but increases the dose delivered to the surrounding healthy tissues.

Example 1: Uniform Dose Delivery. We let $\Omega_T = [3, 6]$ and $\Omega_H = X \setminus \Omega_T$. The weighting function is chosen as described in Equation 37, with $w_T = 1$ and $w_H = 0$. For this example, we set $N_y = 30$, with beam energies E_i selected such that their ranges are equally spaced in $[z_{\text{prox}}, z_{\text{dist}} + \frac{1}{4}]$, and set $\sigma_i^2 = 1$ for all i . The admissible set Y is defined as:

$$(41) \quad Y = \{\mathbf{y} \in \mathbb{R}^{N_y} : y_i \geq 0 \ \forall i\},$$

to enforce non-negativity of beam intensities.

In practice, it is typical to deliver a homogeneous dose to the tumour region [41]. As a first numerical experiment, we define the target dose profile as:

$$(42) \quad T(z) = \begin{cases} 1 & \text{for } z \in \Omega_T, \\ 0 & \text{otherwise,} \end{cases}$$

and aim to find parameters \mathbf{y} such that:

$$(43) \quad \|w(x)^{1/2} (D(\mathbf{y}, z) - T(z))\|_{L^2} \rightarrow \min.$$

The optimisation problem is solved using the Broyden–Fletcher–Goldfarb–Shanno (BFGS) algorithm. Results are shown in Figure 18. The solution achieves highly uniform coverage of the target region. Specifically, if \mathbf{y}^* is the optimal set of parameters, the relative error satisfies:

$$(44) \quad \frac{L(\mathbf{y}^*)}{L((0, 0, \dots, 0))} \approx 10^{-6},$$

where:

$$(45) \quad L((0, 0, \dots, 0)) = \int_X w(z)T(z)^2 dz.$$

To provide a visual representation of the optimisation process and the resulting dose distribution, Figure 16 illustrates the input beam configuration, the fluence in depth-energy space, and the final dose profile for Example 1. This figure parallels the visualisation provided earlier for the pristine Bragg peak (see Figure 5), extending to the optimised spread-out Bragg peak (SOBP) used in this treatment plan. This visualisation connects the optimised input beam parameters to the resulting dose distribution.

Example 2: Organ at Risk (OAR). In this example, we retain the tumour region $\Omega_T = [3, 6]$ but introduce an organ at risk (OAR) in $\Omega_O = [6, 8]$. The weighting function w is modified to penalise dose delivered to the OAR, and is defined as:

$$(46) \quad w(z) = \begin{cases} w_T = 1 & \text{for } z \in \Omega_T, \\ w_O = 10 & \text{for } z \in \Omega_O, \\ w_H = 0 & \text{otherwise.} \end{cases}$$

As in Example 1, we set $N_y = 30$ and select beam energies such that their ranges are equally spaced in $[z_{\text{prox}}, z_{\text{dist}} + \frac{1}{4}]$.

The results of this optimisation are shown in Figure 19. The competing objectives of delivering sufficient dose to the tumour while sparing the OAR result in less uniform dose coverage within the tumour region. Compared to Figure 18, there is a notable reduction in LET near the distal edge of the tumour, accompanied by a significant decrease in dose delivered to the OAR. However, this optimisation introduces oscillations and slight under-dosing in the tumour’s distal region, which may be clinically relevant depending on the treatment context.

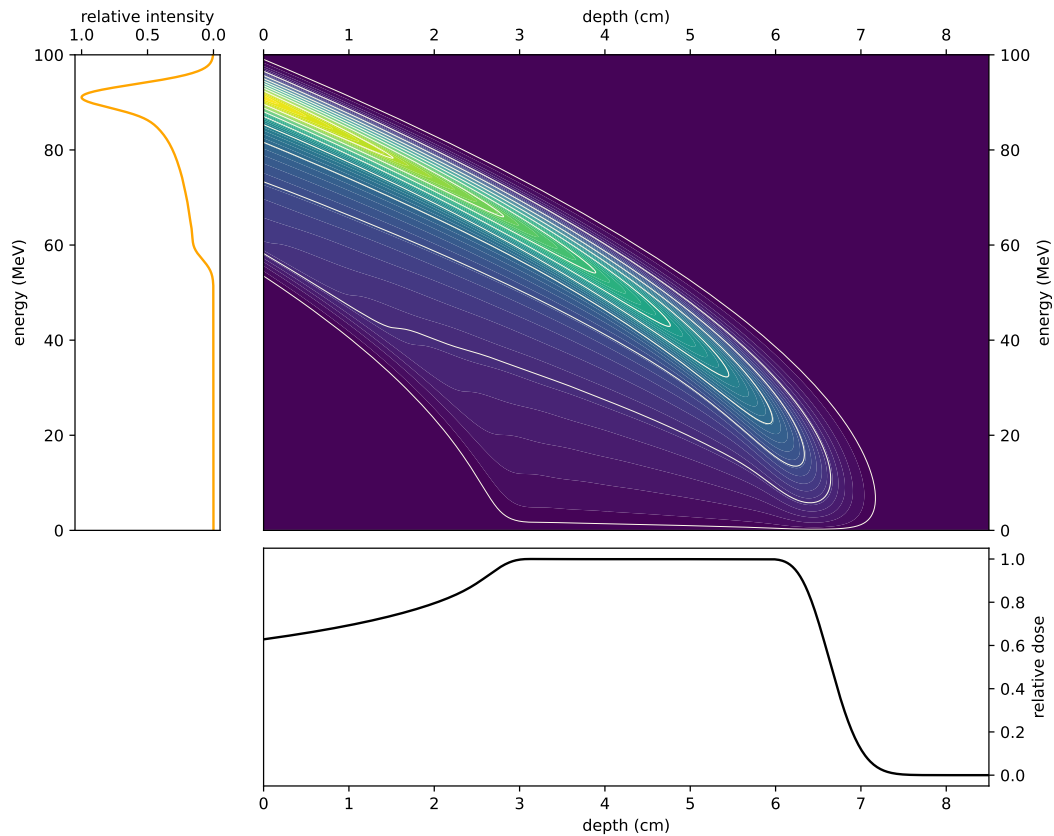


FIGURE 16. Visualisation of the input beam, fluence, and dose profile for Example 1. Left: the optimised input beam intensities across different energies. Middle: the fluence in depth-energy space, showing how the superposition of beams evolves through the medium. Right: the resulting dose profile as a function of depth, achieving a uniform dose within the target region Ω_T .

To further understand the implications of model uncertainty, we examine the effects of parameter variability on the spread-out Bragg peak (SOBP) for a scenario that includes an OAR. Figure 20 shows the Monte Carlo-estimated confidence intervals for both the SOBP and the corresponding dose-averaged LET. The methodology follows that described in section 4, where uncertainty in the stopping power parameters α and p is introduced, and empirical confidence intervals are computed from 25,000 independent samples.

The results highlight significant uncertainty in the maximum dose attained within the SOBP, as well as in the falloff region beyond the tumour. Similarly, there is substantial uncertainty in LET, particularly near the depth where the LET curve becomes sharply peaked. These uncertainties are clinically important to consider in treatment planning, as they heavily affect the balance between

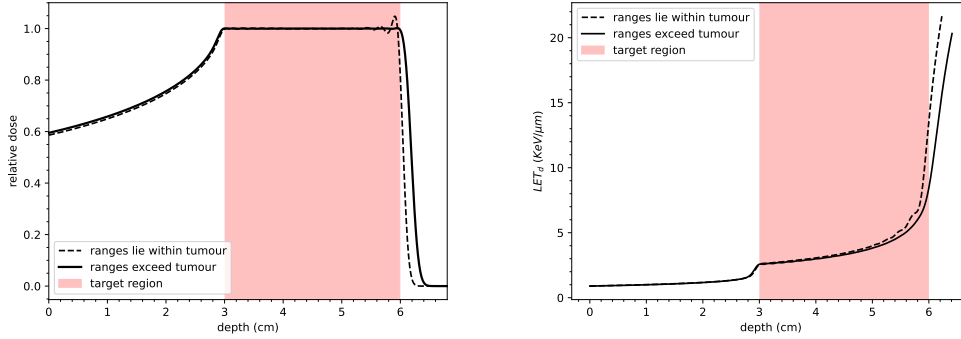


FIGURE 17. Spread-out Bragg peaks (left) and dose-averaged LET curves (right) resulting from the optimisation problem 5.2. Dashed lines: beam ranges are equally spaced between z_{prox} and z_{dist} . Solid lines: beam ranges are equally spaced between z_{prox} and $z_{\text{dist}} + 0.15$. Allowing slight extension of ranges into healthy tissue improves dose uniformity within the tumour.

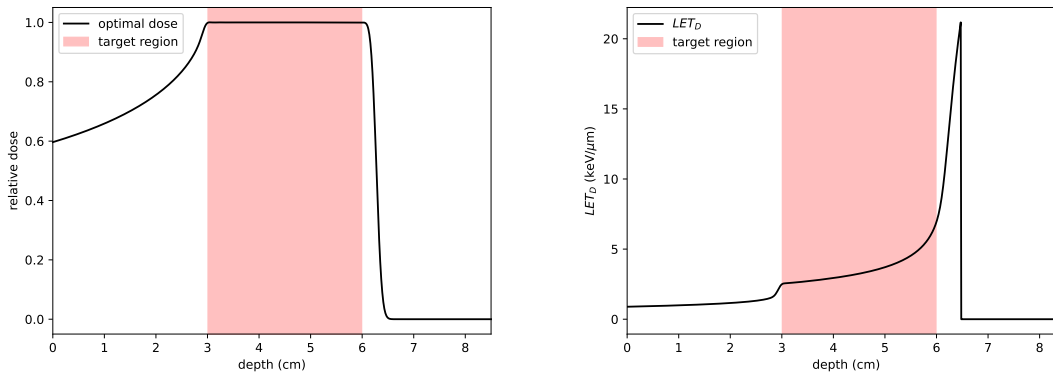


FIGURE 18. Left: dose profile resulting from the optimisation in Example 1. Right: corresponding dose-averaged LET. A total of 30 energy levels are used, with energies chosen such that their ranges are equally spaced and cover the target region. Uniform dose delivery to the tumour is achieved.

tumour coverage and OAR sparing. When an OAR is located directly behind the tumour, such uncertainties can compound the challenge of achieving an optimal treatment plan.

5.5. Optimisation Based on Biological Metrics. An alternative approach to treatment planning involves prescribing the fraction of surviving cells as a function of space, aligning the optimisation process more closely with biological outcomes. For instance, one could aim to kill 90% of

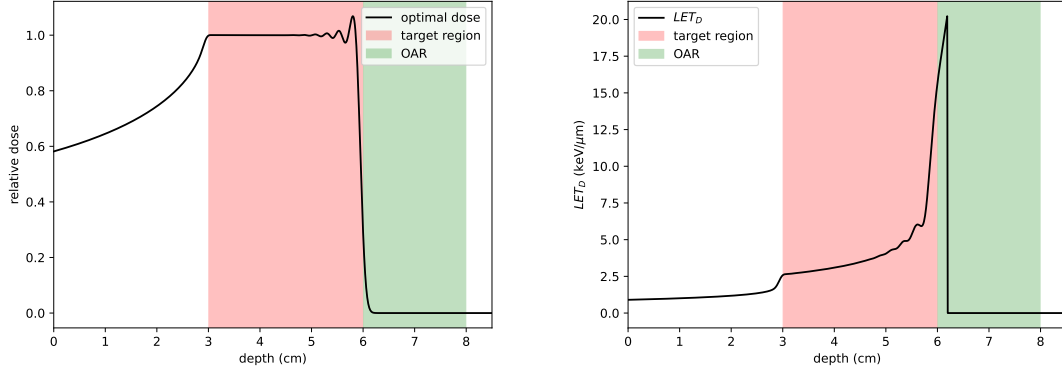


FIGURE 19. Left: dose profile resulting from the optimisation in Example 2. Right: corresponding dose-averaged LET. Penalising dose in the OAR (shaded green) reduces dose penetration into healthy tissue but introduces slight under-dosing and oscillation in the tumour’s distal region.

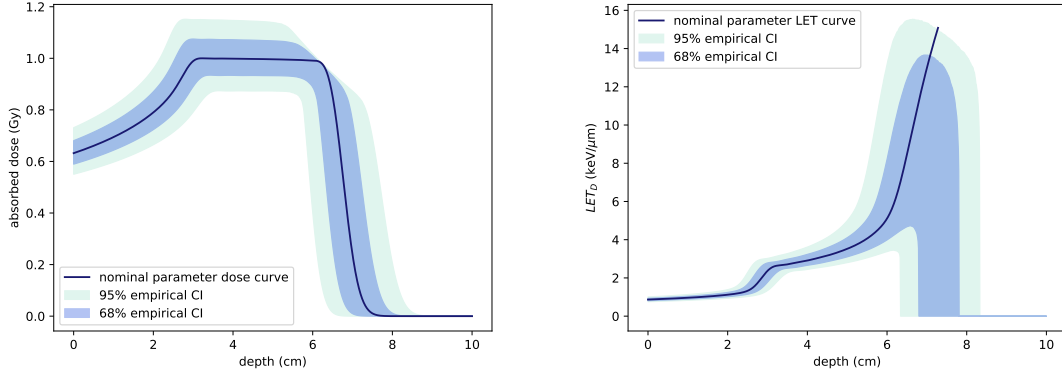


FIGURE 20. Confidence intervals for a spread-out Bragg peak and the corresponding dose-averaged LET. The confidence intervals are obtained as in section 4, by introducing uncertainty in the stopping power parameters α and p , and estimating the empirical confidence intervals from 25,000 independent samples using Monte Carlo methods. The dark blue curves represent the nominal dose and LET profiles, calculated using the assumed parameter values μ_α and μ_p .

cells within the tumour, resulting in an objective function of the form:

$$(47) \quad L_{\mathcal{SF}}(\mathbf{y}) := \sum_{j=1}^{N_x} \frac{1}{2} (w(z)(\mathcal{SF}(\mathbf{y}, z) - T_{\mathcal{SF}}(z))^2) (z_j - z_{j-1}),$$

where $\mathcal{SF}(\mathbf{y}, x)$ denotes the survival fraction and $T_{\mathcal{SF}}(x)$ represents the target survival fraction.

While this approach is biologically motivated, it presents practical challenges. Due to the exponential relationship between dose and survival fraction, the optimisation problem becomes more computationally expensive and can sometimes yield counterintuitive results. For instance, regions receiving excessive dose may not incur a significant penalty in the objective function, as the survival fraction in those regions is already near zero.

To address these limitations, a biologically weighted dose metric is often preferred. By incorporating biological weighting factors into the dose, the optimisation problem becomes linear in terms of the control parameters, significantly reducing computational cost. Moreover, this approach avoids the spurious results associated with excessive dose regions, providing a more robust framework for treatment planning while retaining a biologically informed perspective.

Example 3: Uniform LET-Weighted Dose. In this example, we optimise for a uniform biological dose within the target region Ω_T , defined as:

$$(48) \quad T_{BD}(z) := \begin{cases} 1 & \text{for } z \in \Omega_T, \\ 0 & \text{otherwise.} \end{cases}$$

The input beams are chosen as in Examples 1 and 2, with the weight function w set to $\mathbb{1}_{\Omega_T}$. The results of this optimisation are shown in Figure 21. Optimising for biological dose introduces a trade-off: some dose conformity is sacrificed at the distal part of the tumour to account for the higher LET values that occur there. Consequently, the dose delivered is significantly lower than that obtained by considering absorbed dose alone, reflecting the heightened biological impact of protons near the Bragg peak.

Interestingly, the largest biological effect, computed using the linear-quadratic model, is observed outside the target region when LET is taken into account, as shown in Figure 22. This arises because the LET-weighted optimisation naturally prioritises regions of higher biological effectiveness, even if they fall outside the prescribed dose boundaries. A comparison of the survival fraction profiles resulting from absorbed dose and biological dose optimisation demonstrates this effect. The tapering of the dose profile towards the distal end of the target region ensures significantly less dose is delivered to healthy tissue, while maintaining a near-uniform biological effect within the tumour.

It is instructive to compare these results with those in Figure 4 of [46], where a similar shape is observed in RBE-weighted dose curves. The survival fraction profiles in Figure 22 exhibit a comparable trend, underscoring the alignment between LET-weighted dose optimisation and RBE-based approaches in clinical practice.

6. CONCLUSION

In this work, we have developed a computationally efficient framework for evaluating key metrics in PBT, including dose delivery, LET and biologically informed metrics such as RBE and cell survival fraction. Leveraging a simple analytical model, we achieve results that show good agreement with those from computationally intensive Monte Carlo particle simulations, while significantly reducing computational cost. This makes the framework particularly well-suited for rapid evaluations in treatment planning.

The speed and simplicity of the approach enable the exploration of optimisation strategies with respect to challenging objectives, such as LET-weighted dose or survival fraction. Such objectives, while important for improving treatment outcomes, would require significant computational resources if approached using Monte Carlo simulations. Our framework allows for the efficient evaluation of these biologically informed metrics, providing a practical tool for exploring their potential

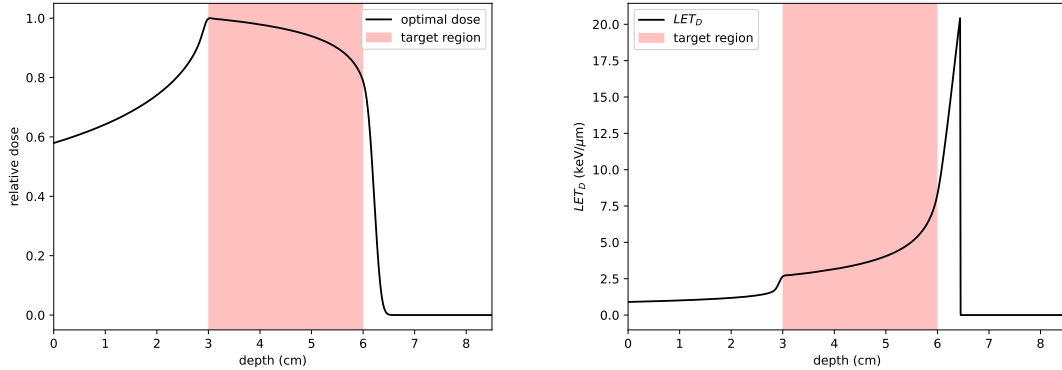


FIGURE 21. Left: dose profile resulting from the optimisation in Example 3. Right: corresponding dose-averaged LET. A total of 30 energy levels are used, with energies chosen such that their ranges are equally spaced and cover the target region.

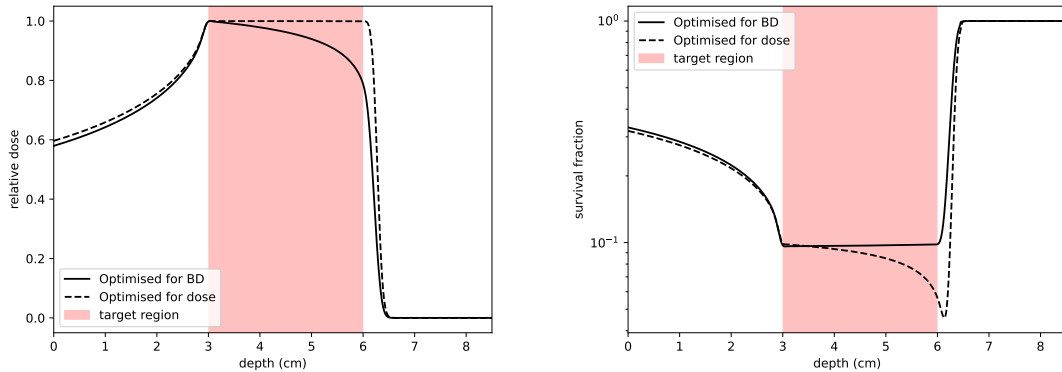


FIGURE 22. Comparison of relative dose (left) and survival fraction profiles (right) resulting from optimisation for absorbed dose (dashed line) and biological dose (solid line). The survival fraction was computed using the linear-quadratic model, with the α parameter accounting for LET, for AG01522 cells using parameters from [8]. Optimising for biological dose results in a tapered dose profile at the distal end of the target region, delivering significantly less dose to healthy tissue while maintaining an almost constant biological effect within the target.

integration into treatment planning workflows as well as for investigating the impact of model uncertainty, particularly in scenarios involving OARs.

By presenting these ideas in a mathematically rigorous but approachable way, we believe this work also serves as an accessible introduction for mathematicians interested in contributing to the field of PBT. The integration of physical, biological and computational principles offers a clear

pathway for mathematical researchers to engage with and address real-world challenges in cancer therapy.

This work demonstrates the value of computationally fast models in bridging the gap between theoretical modelling and practical application in PBT. We believe it provides a foundation for future investigations which account for other interaction mechanisms, Coulomb and nuclear, into biologically informed treatment planning, enabling the rapid assessment of new metrics and strategies that may otherwise be computationally prohibitive, supporting the broader goal of delivering better patient outcomes in personalised cancer therapies.

DATA AVAILABILITY STATEMENT

The codebase used to generate the figures in this work is available at <https://doi.org/10.5281/zenodo.14179258>.

ACKNOWLEDGEMENTS

The research was conducted by a working group sponsored by the Radioprotection theme of the Institute for Mathematical Innovation at the University of Bath. AP and TP were supported by the EPSRC programme grant EP/W026899/1. BA and TP also received support from the Leverhulme Trust grant RPG-2021-238 and TP the EPSRC grant EP/X030067/1. VC is supported by a scholarship through the Statistical Applied Mathematics at Bath (SAMBa) EPSRC Centre for Doctoral Training under the project EP/S022945/1. DH is supported through an NPL iCASE scholarship. All this support is gratefully acknowledged.

REFERENCES

- [1] H. Nystrom et al. “Treatment planning for proton therapy: what is needed in the next 10 years?” In: *The British Journal of Radiology* 93.1107 (2020), p. 20190304.
- [2] F. Salvat. “A generic algorithm for Monte Carlo simulation of proton transport”. In: *Nuclear Instruments and Methods in Physics Research Section B: Beam Interactions with Materials and Atoms* 316 (2013), pp. 144–159.
- [3] K. Jabbari et al. “A fast Monte Carlo code for proton transport in radiation therapy based on MCNPX”. In: *Journal of Medical Physics* 39.3 (2014), pp. 156–163.
- [4] J. Unkelbach et al. “Reoptimization of intensity modulated proton therapy plans based on linear energy transfer”. In: *International Journal of Radiation Oncology* Biology* Physics* 96.5 (2016), pp. 1097–1106.
- [5] M. Frizzelle et al. “Using multi-centre data to train and validate a knowledge-based model for planning radiotherapy of the head and neck”. In: *Physics and Imaging in Radiation Oncology* 21 (2022), pp. 18–23.
- [6] A.-M. Fanou et al. “Implementation, dosimetric assessment, and treatment validation of knowledge-based planning (KBP) models in VMAT head and neck radiation oncology”. In: *Biomedicine* 11.3 (2023), p. 762.
- [7] M. Bellamy et al. “An empirical method for deriving RBE values associated with electrons, photons and radionuclides”. In: *Radiation protection dosimetry* 167.4 (2015), pp. 664–670.
- [8] P. Chaudhary et al. “Relative biological effectiveness variation along monoenergetic and modulated Bragg peaks of a 62-MeV therapeutic proton beam: a preclinical assessment”. In: *International Journal of Radiation Oncology* Biology* Physics* 90.1 (2014), pp. 27–35.

- [9] L. E. Gerweck et al. “Relative biological effectiveness of proton beams in clinical therapy”. In: *Radiotherapy and oncology* 50.2 (1999), pp. 135–142.
- [10] T. Underwood et al. “Variable proton relative biological effectiveness: how do we move forward?” In: *International Journal of Radiation Oncology, Biology, Physics* 95.1 (2016), pp. 56–58.
- [11] D. Giantsoudi et al. “Linear energy transfer-guided optimization in intensity modulated proton therapy: feasibility study and clinical potential”. In: *International Journal of Radiation Oncology* Biology* Physics* 87.1 (2013), pp. 216–222.
- [12] H. Paganetti et al. “Report of the AAPM TG-256 on the relative biological effectiveness of proton beams in radiation therapy”. In: *Medical physics* 46.3 (2019), e53–e78.
- [13] H. Hojo et al. “Difference in the relative biological effectiveness and DNA damage repair processes in response to proton beam therapy according to the positions of the spread out Bragg peak”. In: *Radiation oncology* 12 (2017), pp. 1–9.
- [14] H. Paganetti. “Relative biological effectiveness (RBE) values for proton beam therapy. Variations as a function of biological endpoint, dose, and linear energy transfer”. In: *Physics in Medicine & Biology* 59.22 (2014), R419.
- [15] H. Schättler et al. “Optimal control for mathematical models of cancer therapies”. In: *An application of geometric methods* (2015).
- [16] J.-J. Sonke et al. “Adaptive radiotherapy for anatomical changes”. In: *Seminars in radiation oncology*. Vol. 29. 3. Elsevier. 2019, pp. 245–257.
- [17] H. E. S. Pettersen et al. “Accuracy of parameterized proton range models; a comparison”. In: *Radiation Physics and Chemistry* 144 (2018), pp. 295–297.
- [18] S. N. Boon. “Dosimetry and quality control of scanning proton beams”. In: (1998).
- [19] T. Bortfeld. “An analytical approximation of the Bragg curve for therapeutic proton beams”. In: *Medical physics* 24.12 (1997), pp. 2024–2033.
- [20] W. Ulmer. “Theoretical aspects of energy–range relations, stopping power and energy straggling of protons”. In: *Radiation physics and chemistry* 76.7 (2007), pp. 1089–1107.
- [21] S. Navas et al. “Review of particle physics”. In: *Physical Review D* 110.3 (2024), p. 030001.
- [22] D. J. Thomas. *ICRU report 85: fundamental quantities and units for ionizing radiation*. 2012.
- [23] F. Kalholm et al. “A systematic review on the usage of averaged LET in radiation biology for particle therapy”. In: *Radiotherapy and Oncology* 161 (2021), pp. 211–221.
- [24] K. Souris et al. “Fast multipurpose Monte Carlo simulation for proton therapy using multi-and many-core CPU architectures”. In: *Medical physics* 43.4 (2016), pp. 1700–1712.
- [25] B. Faddegon et al. “The TOPAS tool for particle simulation, a Monte Carlo simulation tool for physics, biology and clinical research”. In: *Physica Medica* 72 (2020), pp. 114–121.
- [26] H. Kooy et al. “Intensity modulated proton therapy”. In: *The British journal of radiology* 88.1051 (2015), p. 20150195.
- [27] T. Kanai et al. “Biophysical characteristics of HIMAC clinical irradiation system for heavy-ion radiation therapy”. In: *International Journal of Radiation Oncology* Biology* Physics* 44.1 (1999), pp. 201–210.
- [28] T. Inaniwa et al. “Reformulation of a clinical-dose system for carbon-ion radiotherapy treatment planning at the National Institute of Radiological Sciences, Japan”. In: *Physics in Medicine & Biology* 60.8 (2015), p. 3271.
- [29] C. P. Karger et al. “RBE and related modeling in carbon-ion therapy”. In: *Physics in Medicine & Biology* 63.1 (2017), 01TR02.

- [30] I. Serrano-Mendioroz et al. “A simple method to assess clonogenic survival of irradiated cancer cells”. In: *Methods in Cell Biology*. Vol. 174. Elsevier, 2023, pp. 127–136.
- [31] A. M. Kellerer et al. “A generalized formulation of dual radiation action”. In: *Radiation research* 75.3 (1978), pp. 471–488.
- [32] L. Hanin et al. “Cell-survival probability at large doses: an alternative to the linear-quadratic model”. In: *Physics in Medicine & Biology* 55.16 (2010), p. 4687.
- [33] K. Chadwick et al. *Molecular theory of cell survival*. Tech. rep. Instituut voor Toepassing van Atoomenergie in de Landbouw, Wageningen . . . , 1973.
- [34] R. B. Hawkins. “A microdosimetric-kinetic theory of the dependence of the RBE for cell death on LET”. In: *Medical physics* 25.7 (1998), pp. 1157–1170.
- [35] D. Goodhead et al. “Direct comparison between protons and alpha-particles of the same LET: I. Irradiation methods and inactivation of asynchronous V79, HeLa and C3H 10T1/2 cells”. In: *International journal of radiation biology* 61.5 (1992), pp. 611–624.
- [36] M. Belli et al. “Inactivation and mutation induction in V79 cells by low energy protons: re-evaluation of the results at the LNL facility”. In: *International journal of radiation biology* 63.3 (1993), pp. 331–337.
- [37] J. Wilkens et al. “A phenomenological model for the relative biological effectiveness in therapeutic proton beams”. In: *Physics in Medicine & Biology* 49.13 (2004), p. 2811.
- [38] N. Tilly. “Radiobiological investigations of proton and light ion therapy”. PhD thesis. Stockholm University, 2002.
- [39] A. Carabe et al. “Range uncertainty in proton therapy due to variable biological effectiveness”. In: *Physics in Medicine & Biology* 57.5 (2012), p. 1159.
- [40] A. Carabe-Fernandez et al. “The incorporation of the concept of minimum RBE (RBE min) into the linear-quadratic model and the potential for improved radiobiological analysis of high-LET treatments”. In: *International journal of radiation biology* 83.1 (2007), pp. 27–39.
- [41] C. Grassberger et al. “Variations in linear energy transfer within clinical proton therapy fields and the potential for biological treatment planning”. In: *International Journal of Radiation Oncology* Biology* Physics* 80.5 (2011), pp. 1559–1566.
- [42] M. McIntyre et al. “A systematic review of let-guided treatment plan optimisation in proton therapy: identifying the current state and future needs”. In: *Cancers* 15.17 (2023), p. 4268.
- [43] T. J. Sullivan. *Introduction to uncertainty quantification / [internet resource]*. eng. 1st ed. 2015.. Texts in applied mathematics ; v. 63. Cham: Springer, 2015. ISBN: 9783319233956.
- [44] W. Chen et al. “A fast optimization algorithm for multicriteria intensity modulated proton therapy planning”. In: *Medical physics* 37.9 (2010), pp. 4938–4945.
- [45] J. Markman et al. “Beyond bixels: Generalizing the optimization parameters for intensity modulated radiation therapy”. In: *Medical Physics* 29.10 (2002), pp. 2298–2304.
- [46] G. Giovannini et al. “Variable RBE in proton therapy: comparison of different model predictions and their influence on clinical-like scenarios”. In: *Radiation Oncology* 11 (2016), pp. 1–16.
- [47] J. Saini et al. “Clinical commissioning of a pencil beam scanning treatment planning system for proton therapy”. In: *International journal of particle therapy* 3.1 (2016), pp. 51–60.

¹INSTITUTE OF MATHEMATICAL INNOVATION, UNIVERSITY OF BATH

²DEPARTMENT OF MATHEMATICAL SCIENCES, UNIVERSITY OF BATH

³DEPARTMENT OF MATHEMATICS AND STATISTICS, UNIVERSITY OF READING